

Characterization of the Bendability of Press-Hardened 22MnB5 Steel

Won Seok Choi and Bruno C. De Cooman*

The bendability of press-hardened 22MnB5 steel was used as evaluation criterion to assess the ability of a press-hardened part to deform plastically in side impact crash conditions. The initiation sites of crack initiating shear bands during the bending operation of press-hardened 22MnB5 steel were found to be formed by surface roughening. Uncoated press-hardened 22MnB5 steel is subject to decarburization and oxidation phenomena occurring during austenitization. These surface processes were found to have a pronounced influence on the bendability of the steel, but their influence on the tensile properties was negligible. Decarburization has a positive influence on bendability by softening the outer sheet surface. Austenitization times prior to press forming in excess of 10 min, resulted in the formation of a surface oxide layer which suppressed the continuation of the decarburization and resulted in the re-homogenization of the carbon concentration profile in the subsurface region. As a result, the decarburization layer was gradually removed, and the bendability of the press-hardened 22MnB5 steel was reduced.

1. Introduction

Press hardening, which is also known as hot press forming, has become a widely used press forming method to produce ultra-high strength steel parts without spring-back.^[1] The press-hardenable steel can be press formed into complex parts due to its initial low strength and high ductility during austenitization, and it is simultaneously hardened by the martensite transformation during rapid cooling in the water-cooled press forming dies. Press-hardened steel parts are used mainly for structural and anti-intrusion parts in automotive body-in-white applications. The number of structural and anti-intrusion application produced with advanced high strength steels has increased substantially due to recent regulatory requirements and corporate safety targets.^[2] Introduction of press-hardened steel in automotive body parts has been shown to improve passenger safety considerably and it has resulted in an increase of vehicle fuel efficiency by weight reduction.^[3]

In industrial practice, the strength and ductility of a flat rolled steel grade are usually measured by means of a standardized tensile test. In case of press-hardening steel (PHS), the ultimate tensile strength (UTS) is about

1500 MPa and total elongation is typically about 7% in the press-hardened state. Information of the crash performance of automotive steel grades has been obtained by standardized full-scale crash tests, drop weight test on welded box-shaped pressed parts or high strain rate tensile tests. Till et al.^[4] and Manuel et al.^[5] have shown convincingly that there was a clear relationship between full-scale crash test results and the bendability of press-hardened steel, and suggested that bendability test results could be sufficiently representative of the crash performance of parts. The results of the bendability test have been shown to be closely related to the crash performance of press-hardened automotive steel. The test can therefore be used to evaluate and improve the ability of a press-hardened part to deform plastically in car collision conditions.

The fracture mechanism in the plane strain bending strain has been investigated in the past. Tvergaard^[6] and Triantafyllidis et al.^[7] analyzed the development of shear bands during bending deformation. They reported that the crystallographic texture had a clear influence on the bending test results and used finite element analysis to study shear band formation. Dao and Li^[8] studied the effect of strain hardening and crystallographic texture on the bendability both experimentally and numerically. They reported that precipitates played an important part in shear band formation. Surface roughening has also been identified as an essential factor in shear band formation, as roughness features are sites where the strain is localized and where cracks can be initiated.^[6–9] Westermann et al.^[9] showed experimentally that the formation of shear band was influenced by the microstructure and the

[*] W. S. Choi, B. C. De Cooman
Graduate Institute of Ferrous Technology, Pohang University of Science and Technology, Pohang, Republic of Korea
Email: decooman@postech.ac.kr

crystallographic texture resulting from the rolling and recrystallization process. Yamazaki^[10] emphasized the influence of the homogeneity of ultra-high strength steel on bendability. Steninger and Melander^[11] focused on the effect of metallic and non-metallic inclusions on ductile fracture in bending, and compared their bending results with tensile properties. They showed that the distribution and volume fraction of the inclusions, where the voids were nucleated, determined the ductility in bending. Datsko and Yang^[12] correlated bendability to tensile properties, in particular the reduction in area (RA) at fracture. A similar correlation between bendability and RA was presented by Sakar et al.^[13] The effect of the annealing time and temperature of press-hardened steel on the bendability was also investigated.^[5] Steels heated in an atmosphere containing oxygen were subject to surface oxidation and decarburization.^[14] In a hot stamping line, PHS with different coating systems is used to avoid the harmful influence of the oxidation and decarburization on the surface appearance and the mechanical properties of the parts.^[15] As the bending response of a PHS part depends on its surface properties, these two phenomena are expected to have an important impact on the bendability of an uncoated press-hardened part, which would not be as apparent by testing the PHS in a uniaxial tensile test. Generally, the bendability is defined by the ratio of sheet thickness to punch radius, which can endure a specified bending operation without fracture.^[13,16,17] In the present study, the bending angle at the maximum bending force F_{\max} was considered as the measure of bendability.

The bending fracture mechanism of a PHS was studied experimentally and the effect of the decarburization and the oxidation on the bendability and the surface properties of the PHS 22MnB5 were characterized.

2. Experimental

A 22MnB5 PHS was used in the present study. The steel was prepared by vacuum inducting melting. The composition of the steel is given in Table 1. Boron improves the steel hardenability, i.e. it promotes the transformation of austenite to martensite at relatively low cooling rates by retarding the austenite decomposition to ferrite. The carbon content is determined by the strength required for the lath martensite at room temperature. The cast material was hot rolled, pickled, and cold rolled. The final cold-rolled thickness (t) was 1.5 mm. For the press-

	C	Mn	B	Si	Cr	Ti
22MnB5	0.24	1.22	0.002	0.25	0.16	0.03

Table 1. Composition of 22MnB5 and modified steel (in mass-pct).

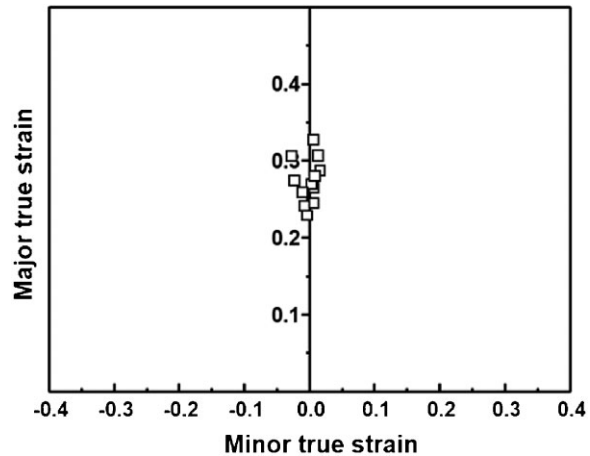


Figure 1. Major strain-minor strain diagram of the strain state on the outer bend in a three points bending test used in the present work. The location of the data points on the major strain axis indicates that the test is a pure plane strain test.

hardening simulations, the steel was heated to 1173 K (900°C), and held for 4, 6, and 10 min in air. A flat die was used to die-quake the specimen without deformation. The three point bending test was carried out according to the ISO7438 standard method. The sample size was

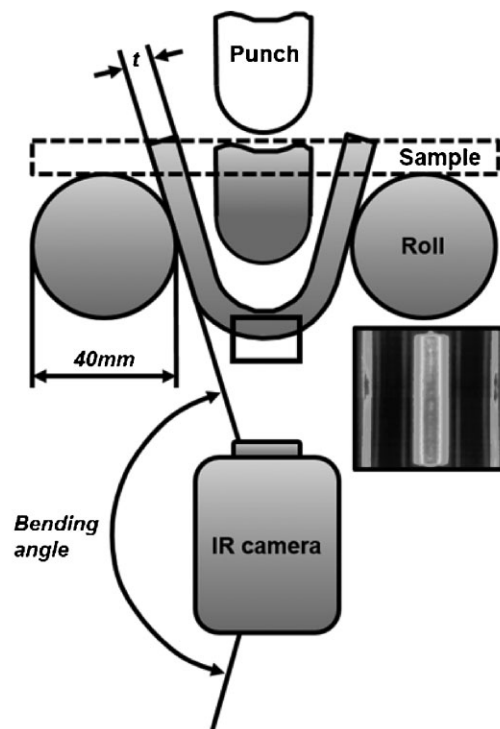


Figure 2. Schematic of the three point bending test equipped with an IR thermography camera to obtain in situ temperature-sensitive images (inset) of the sample outer bend surface which allow for the exact identification of the fracture point and observation of the crack propagation during bending deformation.

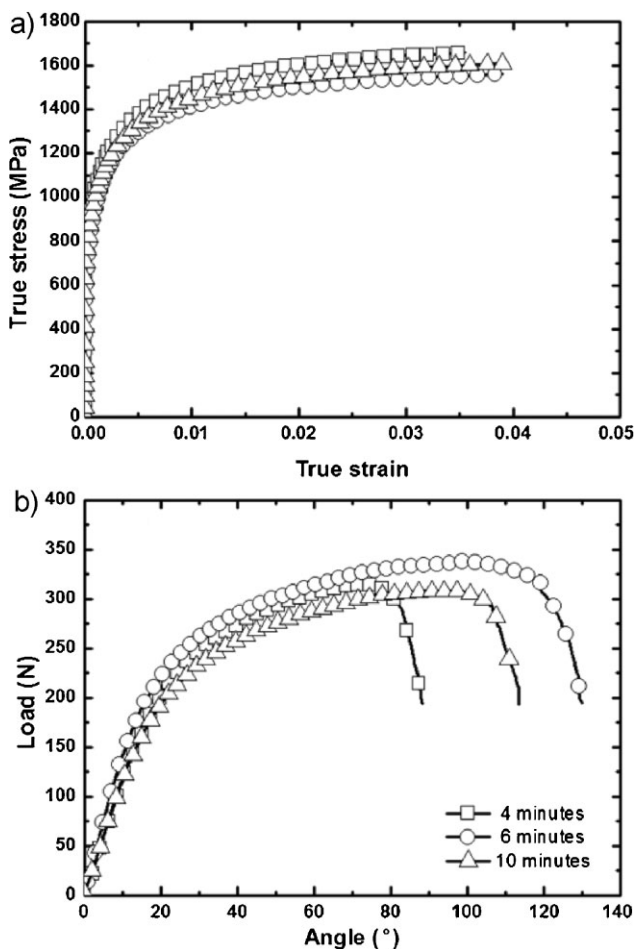


Figure 3. a) Tensile true stress–strain curves and b) bending load versus bending angle curves for press-hardened PHS 22MnB5, austenitized at 1173 K (900°C) for 4, 6, and 10 min.

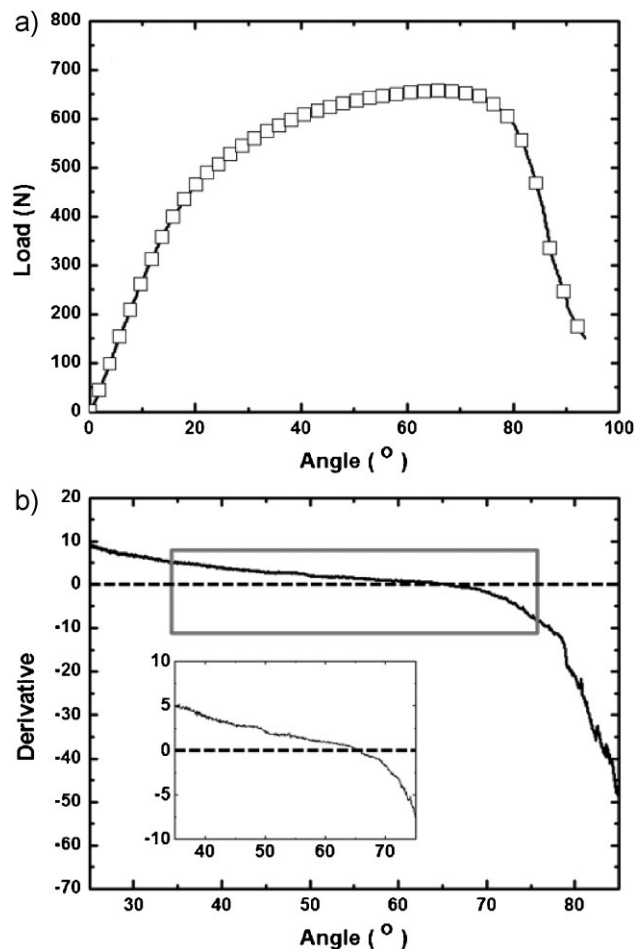


Figure 4. a) Bending load angle curve and b) its derivative curve. The IR thermography of press-hardened steel shows the occurrence of a heat spike resulting from crack initiation and propagation.

20 mm × 60 mm with the longer side of the specimen parallel to the rolling direction (RD). The thickness of the specimen was 1.5 mm. The experiments were conducted with a 20 mm min⁻¹ punch speed. The punch radius was 0.4 mm. The diameter of rollers was 40 mm. A schematic diagram of three point bending test clearly indicates that the bend is subjected to the plane-strain during bending (Figure 1). The test results were plotted in load versus bending angle graphs with the bending angle as defined in Figure 2. An IR camera was also mounted on

the test equipment to obtain in situ temperature-sensitive images of the outer bend surface allowing for an exact identification of the fracture initiation site and the observation of the crack propagation during bending. A schematic of the three point bending test equipped with the IR-thermography camera is shown in Figure 2. Uniaxial tensile tests were carried out on a Z100 ZWICK universal testing machine operated at a constant strain rate of 10⁻³ s⁻¹ using ASTM E-8 standard specimens. The samples, which were given a PHS thermal cycle in a

Heating time [min]	YS [MPa]	UTS [MPa]	UE [%]	F _{max} [N]	Angle _{max} [°]	Fracture point [°]
4	1177	1588	3.56	315	73.3	88.2
6	1094	1490	3.89	337	96.6	130.0
10	1136	1534	3.93	308	92.5	113.5

Table 2. Tensile and bending properties of press-hardened 22MnB5.

N_2 environment, were prepared in a thermal simulator system manufactured by ULVAC-RIKO, INC. The fracture mechanism in bending was analyzed by interrupted experiments. The bending test was interrupted when the bending angle reached 80 and 100% of the angle at the maximum bending force, which was defined as the bendability in the present study, and the experiment was continued until the specimen fractured. The specimen cross sections were observed by scanning electron microscopy (SEM). The SEM observations were carried out on a ZEISS Ultra-55 FE-SEM. The three dimensional analysis of the surface morphology was done using the ROBO-MET 3D automated sectioning equipment in order

to analyze surface roughening of the outer bend surface quantitatively. The three-dimensional image analysis was done with the Avizo 6 software. Samples for 3D surface visualization were polished with a $3\ \mu\text{m}$ diamond suspension. The average layer thickness was approximately $0.5\ \mu\text{m}$. The surface roughening was measured on a $130\ \mu\text{m} \times 310\ \mu\text{m}$ area.

The decarburized layer was studied by SEM and transmission electron microscopy (TEM). Cross sectional samples were etched with a 3% Nital solution for 10 s, and investigated by SEM. The TEM specimens were prepared by the focused ion beam (FIB) technique, and observed in a JEOL JEM-2100F operated at 200 kV.

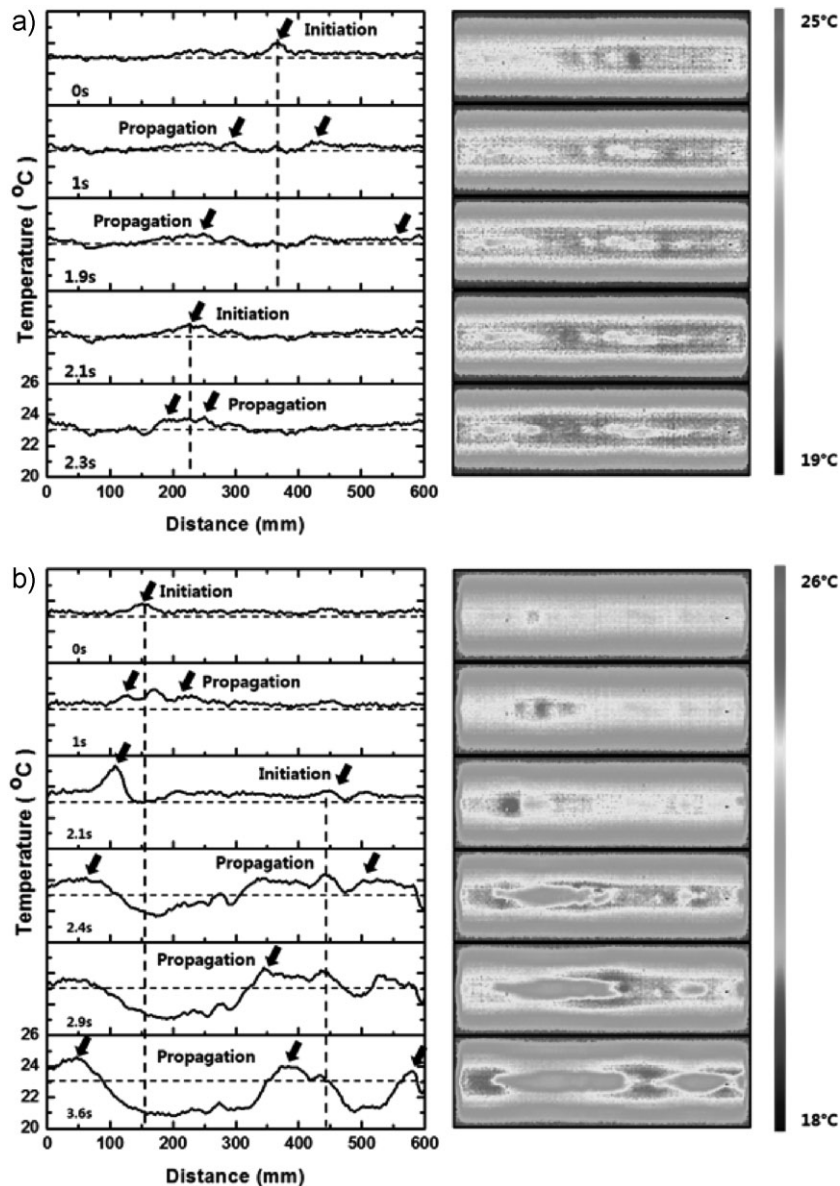


Figure 5. Temperature profile along the outer surface of the bend (left) and the corresponding in situ IR thermography images (right) during bending and crack propagation. a) Sample annealed at 1173 K (900°C) for 4 min and b) sample annealed at 1173 K (900°C) for 6 min. The arrows indicate crack initiation sites and the location of the crack tip during crack propagation.

The carbon concentration profile in the decarburization layer was determined indirectly by means of Vickers microindentation hardness measurement using a Wilson's Tukon-2100B hardness tester. In the case of the microindentation hardness test, which produces indentations with diagonals smaller than about 25 μm , the hardness number is different from macroindentation hardness number obtained according to ASTM E384-11 which uses a higher indenter force ($>1\text{ kgf}$). It is due to a significant effect of the elastic recovery after force removal on the result of microindentation hardness. The mean diagonal length of the indentation was corrected to take the larger elastic recovery into account.

The oxide layer on the press-hardened steel surface was characterized in a JEOL field emission (FE) source electron probe micro analyzer (EPMA) operated at 15 kV.

3. Results

Figure 3a shows the uniaxial tensile true stress–true strain curve for the 22MnB5 PHS grade austenitized at 1173 K (900°C) for 4, 6, and 10 min and die-quenched. The steel heated for 4 min exhibited the highest UTS, followed by the steel heated for 10 min. The uniform elongation (UE) was not influenced by the heating time at 1173 K (900°C). The difference in UTS between the specimens is $<100\text{ MPa}$. Figure 3b shows the bending properties for the hot press formed steel as a function of the heating time. The bending properties of the steel heated for 4 min are clearly lower than the bending properties of the steel austenitized for 6 and 10 min. The bendability was inversely related to the UTS of the press-hardened steel. The bendability was not related to the UE. The F_{max} of the specimen austenitized for 6 min was higher than for the specimens austenitized for 4 and 10 min. The austenitizing time dependence of

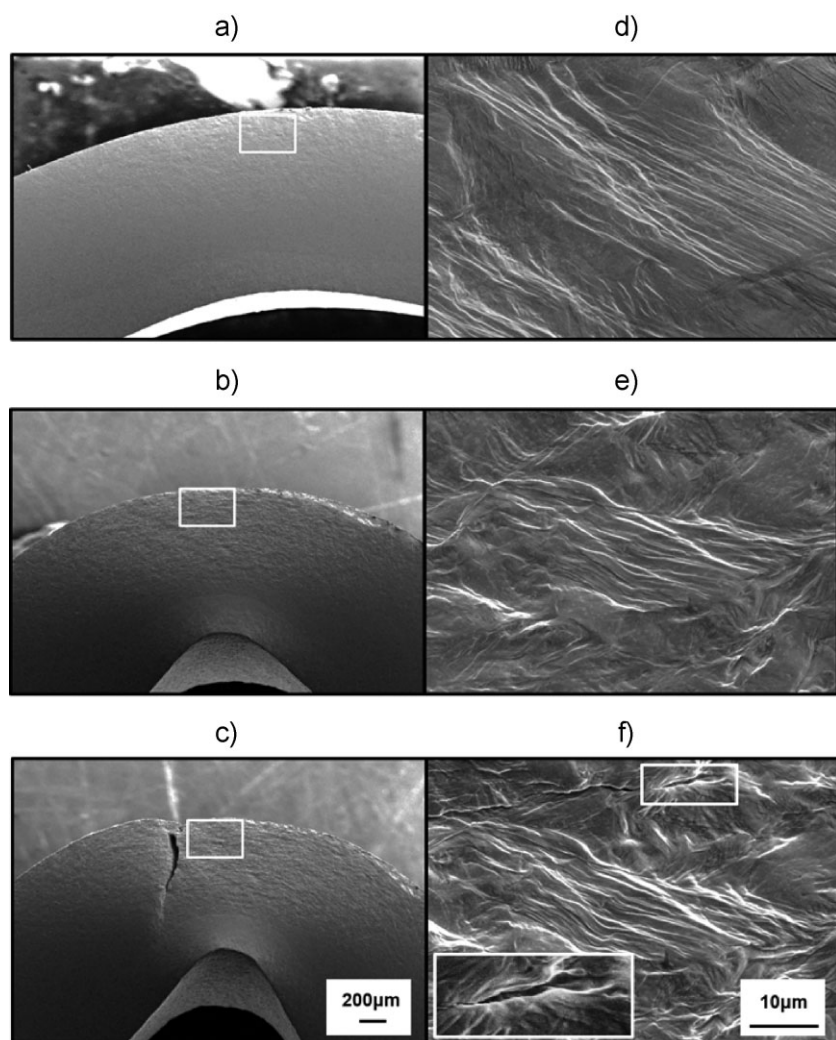


Figure 6. SEM observation of bending samples in interrupted bending test, for a bending angle of a) 80% and b) 100% of the bending angle at F_{max} , and c) for a fractured specimen. Concentrated shear bands are clearly visible near the top surface of the bending specimen: d–f) are enlargements of the boxed regions indicated in a–c), respectively.

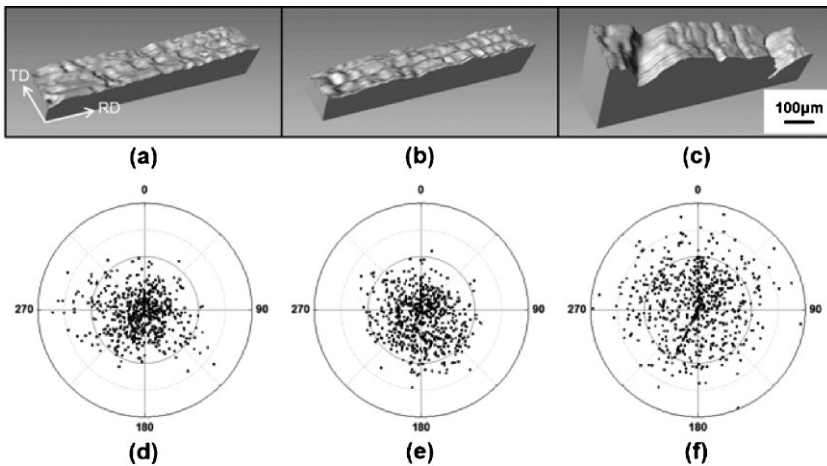


Figure 7. 3D morphology of the surface of a sample bend a) to 80% and b) 100% of the bending angle at F_{\max} , and c) a fractured specimen. The stereographic projections of the surface normal vector of each voxel in (d–f) are for the surfaces shown in a–c), respectively.

the bending curves is quite pronounced in comparison the influence of the austenitizing time on the UTS, which does not show a pronounced heating time dependence. The results of the bending and tensile tests are summarized in **Table 2**.

Figure 4a shows a load versus bending angle curve for the press-hardened 22MnB5 steel. The derivative of the curve is shown in **Figure 4b**. Larger bending test specimens, 50 mm × 60 mm in size were prepared to detect fracture initiation, and the test was carried out with wider roller gap. The outer surface of the bend was then observed by IR thermography. When the derivative load-angle curve shows a sharp drop for bending angles larger than the angle for which the derivative of the force-bending angle curve is zero, a local temperature spike could usually be observed on the IR image of the specimen outer surface (**Figure 4b**). It coincides with the start of the cracking of the specimen in bending.

In situ IR thermography during bending revealed a steady temperature increase with increasing bending deformation. **Figure 5a** and **b** presents the temperature line profile along the middle of the bend and the full IR thermographic image of the bend area at different times for specimens austenitized for 4 and 6 min, respectively. After the load reached its maximum in the load-bending curve, a first crack was formed, which propagated laterally toward the edges of the sample. The temperature spikes indicated by the arrows in the IR thermography data shown in **Figure 5** clearly show that the two crack tips propagated along the bend in the specimen and moved toward the sample edges. The bendability of the specimen heated for 6 min was higher than the specimen heated for 4 min. As a result, **Figure 5b** shows a higher temperature rise with increasing bending angle due to a larger amount of plastic deformation prior to cracking. Since the crack propagation rate in the specimen austenitized for 6 min was slower, the area of the bend where the initial crack was formed cooled down as the

crack widened. As a result, the line temperature profile showed more thermal fluctuation for the specimen austenitized for 6 min than for the specimen austenitized for 4 min.

SEM observations made for interrupted bending test are shown in the **Figure 6**. The observations were made on

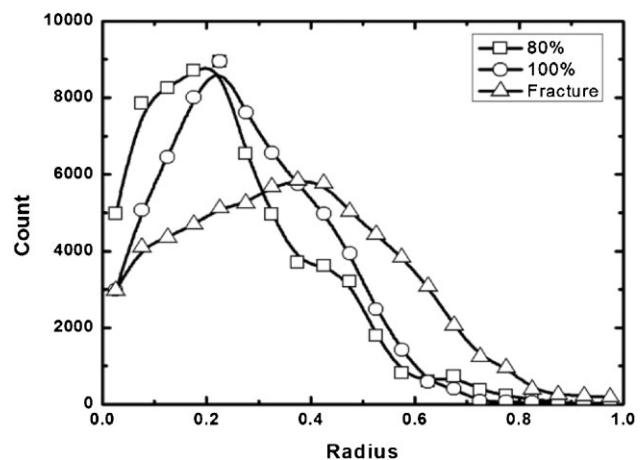


Figure 8. Radial surface normal distribution at 80 and 100% of the bending angle at F_{\max} , and at fracture as determined from the stereographic projection in **Figure 7**. The distribution maximum increases and the distribution becomes more diffuse with increasing bending, indicating a pronounced increase of the surface roughness.

	80%	100%	Fracture
Average of radius	0.25	0.28	0.36
Standard deviation	1393	1696	1717

Table 3. Average value and standard deviation of radius in stereographic projection.

specimens bend by 80%, 100% based on the bending angle at F_{\max} , and on a fractured specimen. In plane strain, the surface of the material is first roughened due to orientation and slip geometry differences between grains. This stage is followed by shear band formation, which results from strain localization induced by the roughening of the outer surface which is subject to the maximum tensile stress^[7,8] In the case of the press-hardened 22MnB5 steel, fracture occurs abruptly without void nucleation and void coalescence as is the case of low carbon cold forming steels.^[11] Concentrated shear bands were formed near the outer

surface of the specimen bend by 80% of the angle at F_{\max} (Figure 6d). The shear band became more roughened as the bending deformation increased. It resulted in microcracks due to strain localization at the shear bands (Figure 6f), and the sudden crack propagation was indicated by a sharp drop in the bending force.

A 3D topographic image of the outer surface roughening of the outer bend surface is shown in Figure 7. Figure 7a–c are for specimens bend by 80%, 100% based on the bending angle at F_{\max} , and on a fractured specimen. The topography of the surface indicates that surface roughening occurred along the rolling direction. The surface continues to roughen after fracture had occurred. The normal vectors for each voxel of the top surface were calculated in order to quantify surface roughening. A two-dimensional stereographic representations of the distribution of the voxel normal is shown in the Figure 7d–f. In case of a flat roughness-free surface, the poles are located at the center of diagram. The distribution of the poles becomes more diffuse when the surface roughness increases. Figure 8 presents the corresponding analysis of the angular spread of the voxel normals. It shows the

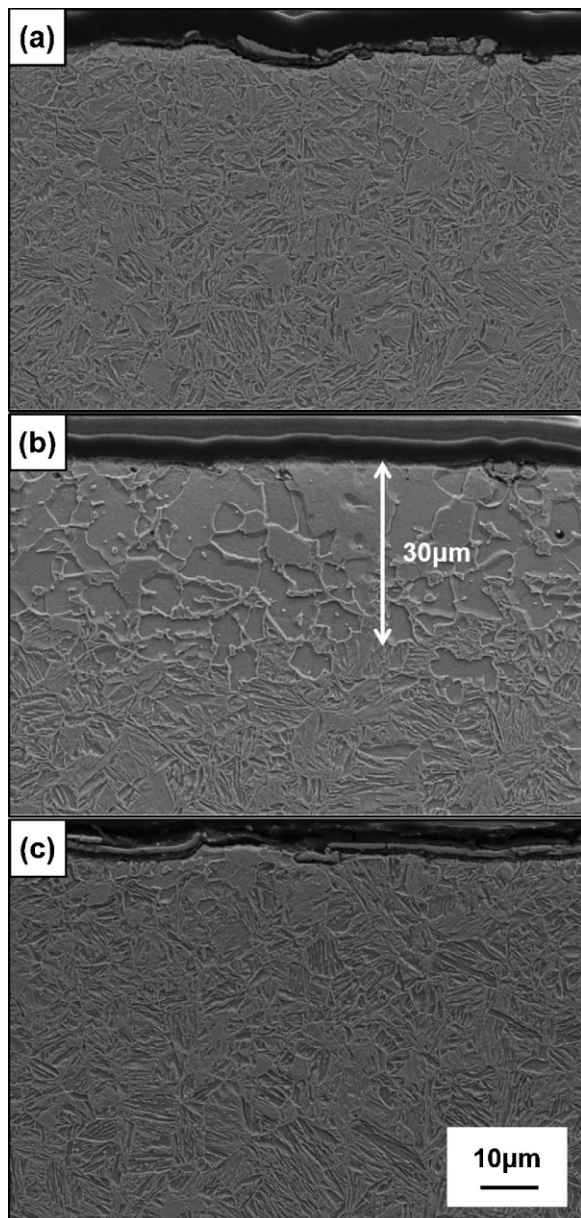


Figure 9. SEM micrographs of 22MnB5 press-hardened steel heated at 1173 K (900°C) for a) 4 min, b) 6 min, and c) 10 min. A decarburization layer with a thickness of 30 μm is clearly visible in b).

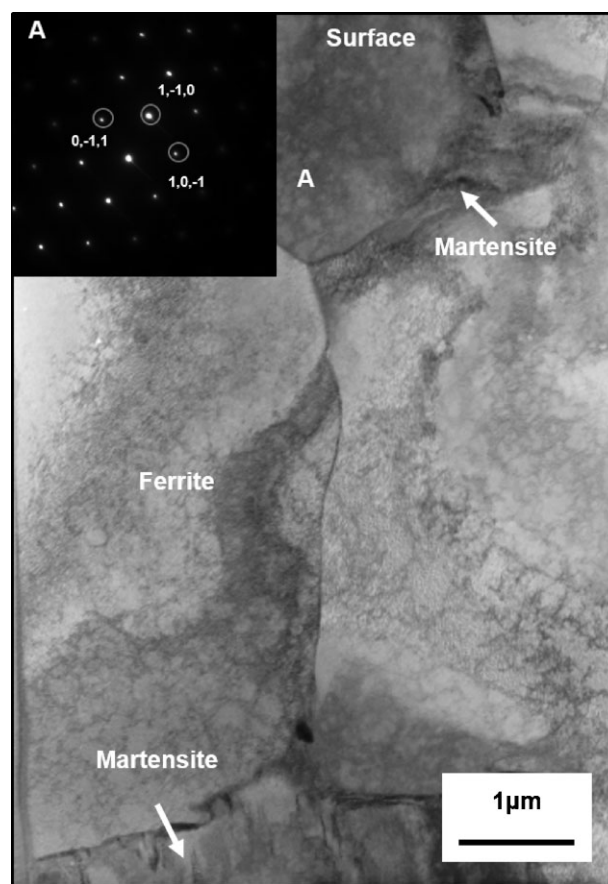


Figure 10. Cross-sectional STEM micrograph of the surface of press-hardened 22MnB5 steel heated at 1173 K (900°C) for 6 min. The decarburization layer consists of ferrite and small-embedded martensite islands indicated by arrows.

density of the voxel poles as a function of their inclination relative to the normal direction. The average and the standard deviation of the inclination versus radius distribution are listed in Table 3. The both values increased with increasing bending angle, indicating that the surface roughening intensified as the bending progressed.

The etched cross sections of the specimens heated for 4, 6, and 10 min are shown in Figure 9. In the case of the sample heated at 1173 K (900°C) for 6 min shown in Figure 9b, a decarburized layer of 30 μm was present at the surface. The specimens heated for 4 and 10 min had a fully martensitic microstructure as can be seen in Figure 9a

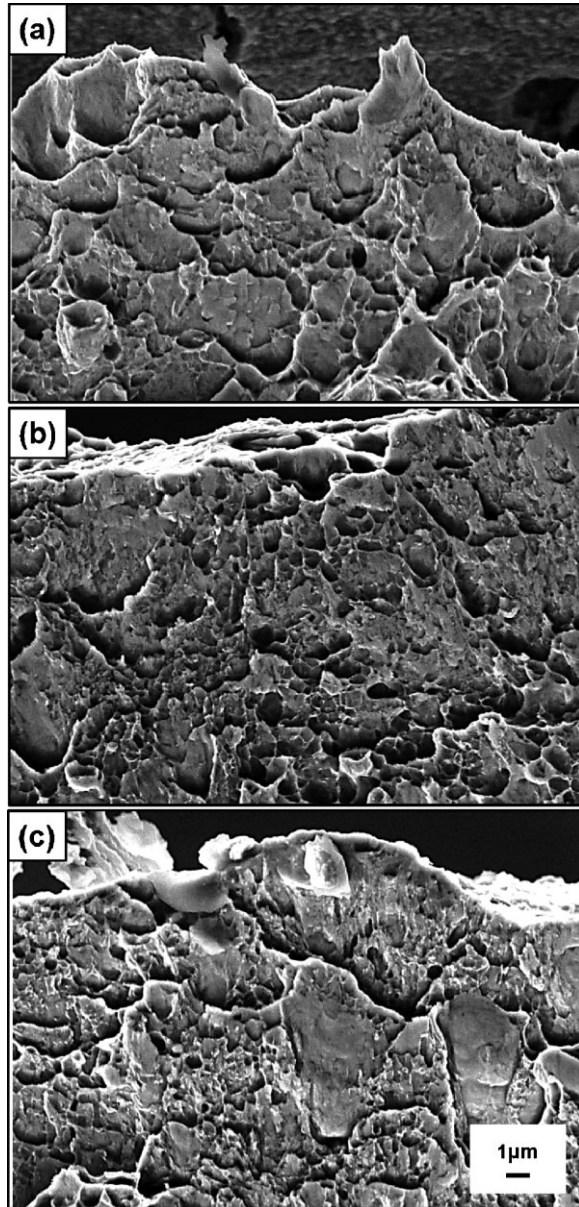


Figure 11. Fractography of bending specimens heated at 1173 K (900°C) for a) 4 min, b) 6 min, and c) 10 min. The decarburization leads to the presence of multiple small dimples in the case of the decarburized surface region in b)

and c. TEM observations were used to verify the presence of the decarburized layer, which consisted entirely of a ferrite matrix and a small number of martensite islands (Figure 10). The decarburized layer affects the fracture mechanism of the press-hardened 22MnB5 steel. Figure 11 shows the fractography of the bended specimen near the surface. The steel austenitized for 4 min showed a transgranular fine faceted fracture mode, which is usually found on the fracture surface of martensitic steels, whereas the fractography of the steel austenitized for 6 min revealed dimples and no transgranular fracture facets. In the case of the sample heated for 10 min, a combination of transgranular fracture facets and dimples were observed. It clearly indicates that decarburization affects the fracture mechanism of the subsurface, which is subjected to the maximum tensile stress in three point bending test.

4. Discussion

Material parameters such as homogeneity and the presence of a banded microstructure are parameters which are known to influence the bendability of advanced high strength steels with a multiphase microstructure.^[10,18] In the case of press-hardened steel, which has a fully martensitic microstructure, these specific parameters do not affect the bendability of the materials. The deformation texture due to cold rolling does also not appear to influence properties due to the randomization of the crystallographic orientations resulting from the austenitization and the subsequent martensitic transformation during the hot stamping process. The steel blanks are heated in air during the hot stamping process, and the oxygen causes surface and subsurface decarburization and surface oxidation. Both phenomena have a direct

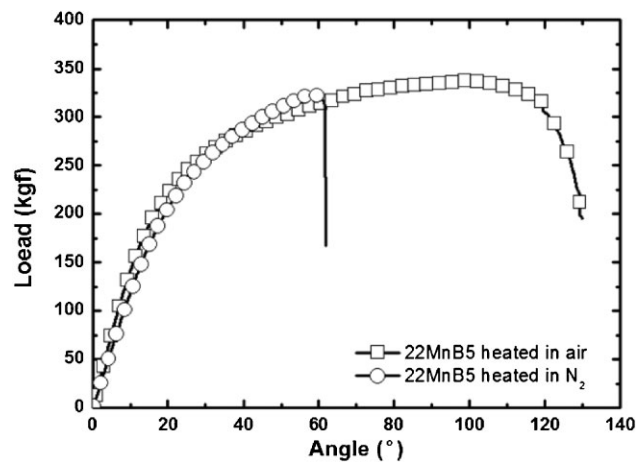


Figure 12. Bending curve for the 22MnB5 PHS steel heated in air and nitrogen at 1173 K (900°C) for 6 min. The decarburization improves the room temperature bendability of the press-hardened steel.

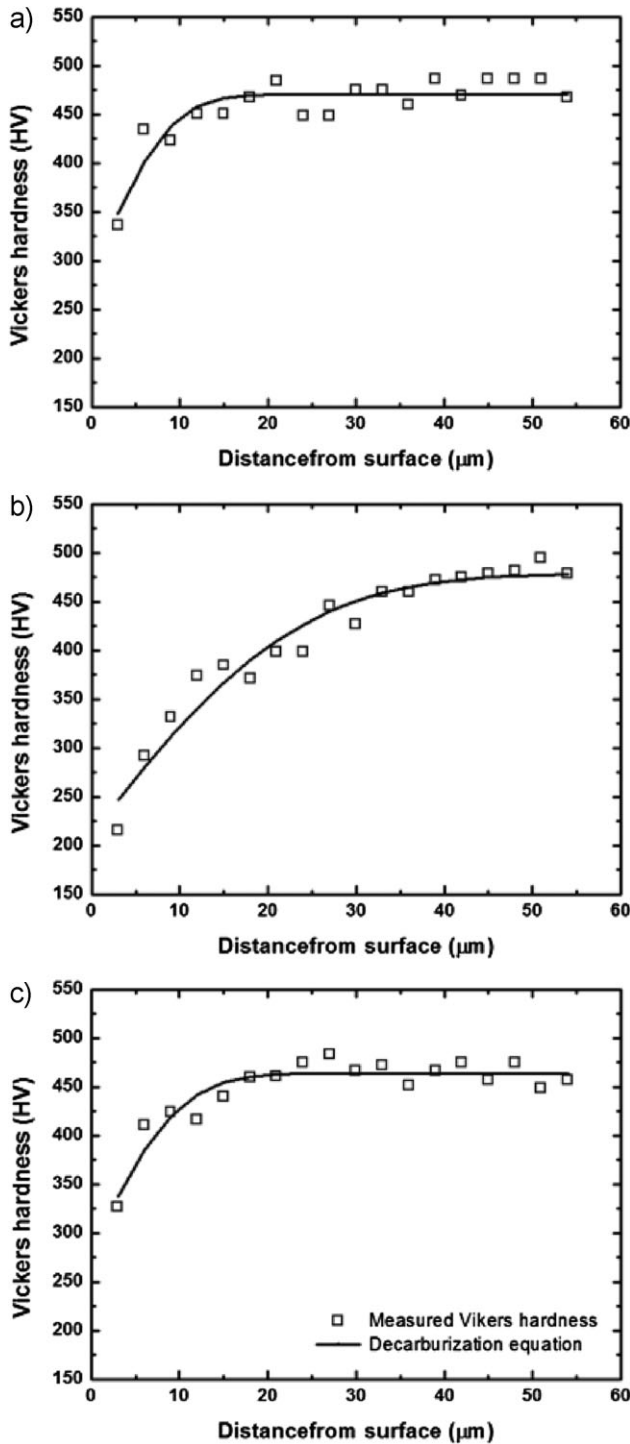


Figure 13. Vickers microindentation hardness value as a function of depth below the surface for press-hardened 22MnB5 austenitized at 1173 K (900°C) for a) 4 min, b) 6 min, and c) 10 min.

influence on the surface appearance and the mechanical properties of a press-hardened part. In plane strain bending specimens subjected to a non-uniform deformation, the bendability of the material is expected to considerably be influenced by these phenomena.

The results in Figure 3 reveal that the decarburization phenomenon affects the bendability of press-hardened steel significantly. In the case of the plane-strain bending test, the surface is subjected to the maximum tensile stress. The stress on the inner surface of the strip sample is compressive. During a tensile test, the specimen is deformed homogeneously prior to necking.^[11] The decarburization occurring during austenitization improves the bendability considerably, whereas the tensile properties are not affected. The bendability was also tested for specimens heated for 6 min in a N₂ gas atmosphere to verify the effect of decarburization on the bendability of hot press formed steel. The results are shown in Figure 12. The bending angle of the steel heated in air is twice that of the steel heated in N₂. The tip of the initial cracks occurring during bending is being blunted in the case of the steel heated for 6 min compared to the other steel. It will be shown that the most likely explanation reason for the deterioration of the bendability for the sample austenitized for 10 min is the re-homogenization of the subsurface carbon content as a result of the surface oxidation.

Interstitial carbon has a major influence on the mechanical strength of the martensite formed by hot press forming and a reduction of the carbon content in the subsurface will reduce the strength of martensite and increase the formability locally. A pronounced decarburization results in the suppression of martensite formation during press hardening and leads to the formation of a much softer ferrite layer. The decarburization depth below the surface of an uncoated press-hardened part can be determined experimentally by means of Vickers microindentation hardness measurement. It is well known that the carbon concentration and the Vickers microindentation hardness of lath martensite are linearly related:^[19]

$$H = m \cdot C + a \tag{1}$$

here H is the Vickers microindentation hardness, C is the carbon content, m and a are constants, which can be determined experimentally. It is also known that the steel decarburization profile obtained by solving Fick's second law of diffusion is given by Ref.^[20]:

$$(C_x - C_s) = (C_o - C_s) \operatorname{erf} \left[\frac{x}{2(D_c^y t)^{1/2}} \right] \tag{2}$$

here C_x is carbon content at a distance x below the surface, C_s is the carbon content at the surface, C_o is the nominal carbon content of the steel, x is the distance from the surface, D_c^y is the carbon diffusivity in austenite, which is $1.21 \times 10^{-11} \text{ m}^2 \text{ s}^{-1}$ at 1173 K (900°C),^[21] and t is the diffusion time. In order to determine the carbon concentration profile, which develops during austenitization at 1173 K (900°C), the Vickers microindentation hardness

Heating time [min]	H_o	H_s	m	a	C_s	Depth of decarburization [μm]
4	477	336	996.2	231.7	0.048	18
6	478	215	1110.2	212.7	0.0	48
10	463	326	994.6	225.2	0.057	21

Table 4. The results of numerical analysis to fit experimentally determined microindentation hardness with decarburization equation.

profiles were measured (Figure 13). Substituting the expression for carbon into Equation 2, the position-dependence of the microindentation hardness is similar to the position-dependence of the carbon content because of the linear relationship between microindentation hardness and carbon content:

$$(H_x - H_s) = (H_o - H_s) \operatorname{erf} \left[\frac{x}{2(D_c t)^{1/2}} \right] \quad (3)$$

here H_x is the microindentation hardness at a distance x , H_s is the surface microindentation hardness, and H_o is the microindentation hardness in a region unaffected by the decarburization. The decarburization depth, which is defined as the distance from the surface where carbon content reaches that of the base material, was determined by fitting the measured hardness values to Equation 3 (Figure 13). The distance, where a hardness value of $0.99 H_o$ was obtained, was considered as the depth of decarburization. It corresponds to a depth of about $50 \mu\text{m}$ in the case of the steel austenitized for 6 min. The depth of decarburization of the steel austenitized for 4 and 10 min is about $20 \mu\text{m}$. Figure 3 shows that the bendability after a 4 min austenitization is not as good as after a 10 min austenitization. Both materials had a similar depth of decarburization. The fracture surface of the steel austenitized for 10 min showed a combination of transgranular fracture facets and dimples. The fracture surface of the steel heated for 4 min revealed a finely faceted transgranular structure (Figure 11). Ferrite grains, formed in the surface region as a result of the steel decarburization during the 10 min austenitization, appear to be the main cause of the difference in fracture mechanism and bendability. The results of the numerical analysis are listed in the Table 4. The range of the constant m is 994–1110, and the constant a is in the range of 212–231. Using Equation 1 with the results of numerical analysis, the carbon content at the surface C_s for each material was calculated to be 0.049, 0.0, and 0.057 mass% for an austenitization of 4, 6, and 10 min, respectively. The results are in agreement with the relationship between Vickers hardness and carbon content of martensite in Ref.^[22]

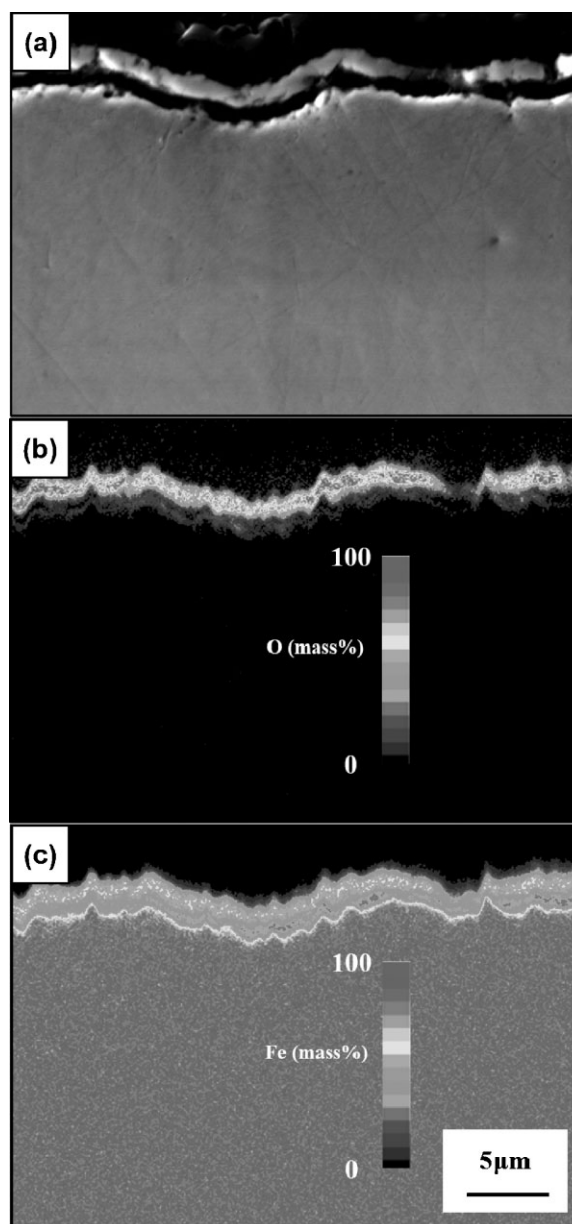


Figure 14. a) Cross-sectional SEM micrograph of the 22MnB5 press-hardened steel heated for 4 min at 1173 K (900°C), and corresponding elemental distribution for b) O and c) Fe.

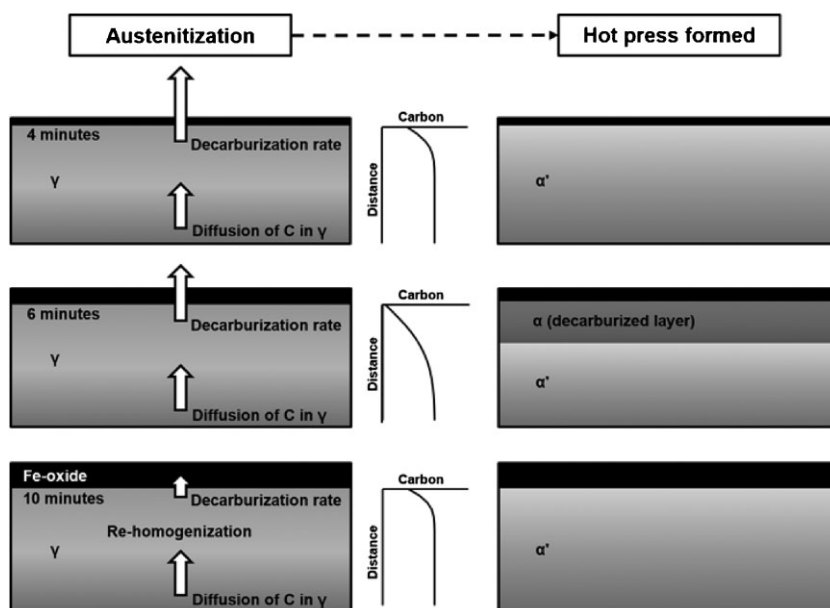


Figure 15. Schematic of the decarburization and the re-homogenization of the carbon profile during the heating prior to press forming of an uncoated PHS steel. The subsurface carbon profile is removed due to the suppression of the surface decarburization resulting from the formation of an iron oxide layer.

The formation of iron oxide at the surface leads to the re-homogenization of the carbon content profile in the subsurface decarburization layer. In the press-hardening process, the steel is heated in air, and the isothermal growth of iron oxide occurs at the steel surface during the temperature homogenization. The growth rate of the iron oxide FeO has a parabolic time dependence indicative of a diffusion-controlled growth.^[23] The diffusion of carbon through the scale is very limited since the solubility of carbon in iron oxide is low. As a consequence, the scale acts as an effective obstacle to decarburization.^[24] The decarburization rate is greatly reduced as the iron oxide growth progresses. As the diffusion of carbon in austenite is faster than the decarburization rate, the carbon content in the subsurface region will increase again, and the martensitic transformation will reappear during the quenching step. The EPMA results show that the iron oxide covers the steel surface (Figure 14). The chemical composition of the oxide was close to that of FeO, which is usually the main oxide constituent of scale formed on low carbon steels at 900°C. A schematic illustrating the decarburization and re-homogenization during hot press forming process is shown in Figure 15. It describes the decarburization and the re-homogenization of the carbon profile during the heating prior to the press hardening of an uncoated PHS 22MnB5. The subsurface carbon profile is removed due to the suppression of the surface decarburization resulting from the formation of an iron oxide layer. It is clear that the softening of the subsurface, due to decarburization, and the possible re-homogenization of carbon profile, due to the surface oxidation, can be the cause of significant variation in the bendability of uncoated PHS 22MnB5.

5. Conclusions

The effect of decarburization and oxidation during the temperature homogenization stage of the press-hardening process on the bending fracture mechanism of uncoated cold-rolled PHS 22MnB5 was analyzed. The main results of the present study are as follows:

1. Surface roughening increased during the bending operation. Shear bands were formed at stress-concentrating features on the roughened surface. The strain localization due to the presence of the shear bands initiated the crack formation.
2. In the hot stamping process, the high temperature of austenitization, 1173 K (900°C) in air, resulted in the surface decarburization and oxidation. A decarburized layer 30 μm in thickness was clearly observed at the surface, and the total decarburization depth was about 55 μm. The presence of the decarburized surface layer had a significant influence on the bending properties of the press-hardened steel, but the tensile properties were not affected.
3. The re-homogenization of the subsurface carbon content takes place after the formation of the Fe-oxide layer at the surface, which prevents the further decarburization.

The results strongly suggest that the bendability of uncoated press-hardened steel is influenced by the decarburization and oxidation processes occurring at the steel surface in the heating stage of the hot stamping process.

Received: July 12, 2013;
Published online: January 14, 2014

Keywords: press hardening; 22MnB5; three point bending; decarburization

References

- [1] H. Karbasian, A. E. Tekkaya, *J. Mater. Process. Technol.* **2010**, *210*, 2103–2118.
- [2] M. Merklein, J. Lechler, *J. Mater. Process. Technol.* **2006**, *177*, 452–455.
- [3] M. Kleiner, M. Geiger, A. Klaus, *CIRP Ann. Manufact. Technol.* **2005**, *52*, 521–542.
- [4] L. Till, P. Markus, 1st Int. Conf. Hot Sheet Metal Forming of High-performance Steel, CHS², Kassel, Germany, 2008, pp. 143–151.
- [5] M. Manuel, C. Jorg, S. Monika, K. Steffen, A. Michael, S. Kurt, 3rd Int. Conf. Hot Sheet Metal Forming of High-performance Steel, CHS², Kassel, Germany, 2011, pp. 49–55.
- [6] V. Tvergaard, *Int. J. Fract.* **1981**, *17*, 389–407.
- [7] N. Triantafyllidis, A. Needleman, V. Tvergaard, *Int. J. Solids Struct.* **1982**, *18*, 121–138.
- [8] M. Dao, M. Li, *Phil. Mag. A* **2001**, *81*, 1997–2020.
- [9] I. Westermann, K. E. Snilsberg, Z. Sharifi, O. S. Hopperstad, K. Marthinsen, B. Holmedal, *Metall. Mater. Trans. A* **2011**, *42*, 3386–3398.
- [10] K. Yamazaki, ATS Int. Steelmaking Conf. Paris, France, 2003, pp. 779–86.
- [11] J. Steninger, A. Melander, *Scand. J. Metall.* **1982**, *11*, 55–71.
- [12] J. Datsko, C. T. Yang, *J. Manuf. Sci. Eng.* **1960**, *82*, 313–314.
- [13] J. Sarkar, T. R. G. Kutty, D. S. Wilkinson, J. D. Embury, D. J. Lloyd, *Mater. Sci. Eng. A* **2004**, *369*, 258–266.
- [14] G. J. Billings, W. W. Smeltzer, J. S. Kirkaldy, *J. Electrochem. Soc.* **1970**, *117*, 111–117.
- [15] D. W. Fan, B. C. De Cooman, *Steel Res. Int.* **2012**, *83*, 412–433.
- [16] C. Wang, G. Kinzel, T. Altan, *J. Mater. Process. Technol.* **1993**, *39*, 279–304.
- [17] C. Iacono, J. Sinke, R. Benedictus, *J. Manuf. Sci. Eng. Trans. ASME* **2010**, *132*, 0210011–0210019.
- [18] Y. Nagataki, S. Tsuyama, Y. Hosoya, T. Okita, High-Strength Steels Automotive Symp. Proc. **1994**, p. 239.
- [19] R. G. Baggerly, R. A. Drollinger, *J. Mater. Eng. Perform.* **1993**, *2*, 47–450.
- [20] J. H. Brophy, R. M. Rose, J. Wulff, *The Structure and Properties of Materials, Volume II: Thermodynamics of Structure*, John Wiley & Sons, New York, USA **1966**, pp. 75–97.
- [21] H. Jehn, H. Speck, W. Hehn, E. Fromm, G. Hoerz, in *Gases and Carbon in Metals and Physics Data V. XIV*, (Eds: H. Behrens, G. Ebel), Max-Planck-Institut für Metallforschung, Institut für Werkstoffwissenschaften, Stuttgart, Germany **1981**, pp. 5–14.
- [22] R. A. Grange, C. R. Hribal, L. F. Porter, *Metall. Mater. Trans. A* **1977**, *8A*, 1775–1785.
- [23] B. C. De Cooman, J. G. Speer, *Fundamentals of Steel Product Physical Metallurgy*, 3rd ed., AIST, Warrendale, PA **2012**.
- [24] W. E. Boggs, R. H. Kachik, *J. Electrochem. Soc.* **1969**, *116*, 424–430.